Geochimica et Cosmochimica Acta xxx (xxxx) xxx

Contents lists available at ScienceDirect

Geochimica et Cosmochimica Acta

journal homepage: www.elsevier.com/locate/gca

Origin of heavy rare earth elements in highly fractionated peraluminous granites

Chaoxi Fan [a], Cheng Xu [a,b,*], Aiguo Shi [a], Martin P. Smith [c], Jindrich Kynicky [d], Chunwan Wei [a]

[a] Key Laboratory of Orogenic Belts and Crustal Evolution, School of Earth and Space Sciences, Peking University, Beijing 100871, China
[b] Collaborative Innovation Center for Exploration of Nonferrous Metal Deposits and Efficient Utilization of Resources by the Province and Ministry, College of Earth Sciences, Guilin University of Technology, Guilin 540001, China
[c] School of Environment and Technology, University of Brighton, Brighton BN24GJ, UK
[d] BIC Brno, Technology Innovation Transfer Chamber, Brno 61200, Czech Republic

ARTICLE INFO

Article history:
Received 25 June 2022
Accepted 13 December 2022
Available online xxxx
Associate editor: Adam Simon

Keywords:
HREE origin
Peraluminous granite
External fluid metasomatism
HREE deposit
South China

ABSTRACT

Rare earth elements (REEs + Y) play an important role in modern industry. Heavy REEs (HREEs) are particularly critical because of their relative scarcity in nature. Global HREE resources are predominantly present in granitoid weathering crusts in southern China. Although it is well known that REEs are generally enriched in alkaline rocks, in contrast, the parental granitoids in most Chinese HREE deposits are peraluminous. Here, we examined different REE mineral compositions, distribution patterns, and Nd isotope ratios of the granitoid complex in Zudong, South China, whose weathering crusts form the largest HREE deposits globally. The complex is composed of granodiorite, biotite-muscovite, and muscovite alkali-feldspar granites, whose REE patterns change from HREE depletion to enrichment relative to light REEs (LREEs) with increasing negative Eu anomalies. They are not fractional crystallization products from the same parental melts owing to the different zircon U-Pb ages (~191, ~169, and ~154 Ma for granodiorite, biotite-muscovite, and muscovite granites, respectively). However, magmatic zircons from the three types of granitoids show consistent initial Hf isotope compositions [$\varepsilon Hf_{(t)}$ = 3.4 to 8.6], indicating they evolved from the same sources. The granodiorite contains primary LREE minerals with low $\varepsilon Nd_{(t)}$ values (−13.8 to −10.1), decoupled from high zircon Hf isotopes. This indicates a garnet-containing basement source resulted in Lu (HREE) remaining preferentially in the garnet phase, with Hf entering the melt. This contradicts the high HREE concentration recorded in the biotite-muscovite and muscovite granites, which contain abundant HREE minerals associated with muscovite, fluorite, and recrystallized quartz. The whole-rocks and their secondary REE minerals show variable and higher initial Nd isotope ratios [$\varepsilon Nd_{(t)}$ = −3.7 to 2.9 and −11.4 to −7.1 for biotite-muscovite and muscovite granites, respectively] than the early granodiorites and their primary REE minerals, indicating minimal ^{143}Nd was derived from radioactive decay of ^{147}Sm in the basement and wall rocks. This constrained the contribution of external REE-, volatile-rich liquids, which drove the segregation of highly evolved silicate melts from the magma chamber. This increased volatile saturation and fluid exsolution, which may have mobilized the HREEs and metasomatized the granites during their emplacement. Therefore, we infer that external fluid metasomatism appears to be crucial for the HREE enrichment in highly fractionated peraluminous granites.

1. Introduction

Rare earth elements (REEs) are essential strategic resources in high-technology industries and indispensable to the development of renewable energy technologies and low-carbon transportation. This, coupled with a reduction in REE exports from China, which holds 37% of the global reserves of rare earth oxides (U.S. Geological Survey, 2022), has imposed the need for REE resource exploration and research. Heavy REEs (HREEs: Gd-Lu + Y) are rarer than light REEs (LREEs: La-Eu) because of their low crustal abundance and limited reserves (Simandl, 2014). HREEs are predominantly derived from exogenous rare earth deposits, particularly regolith-hosted ion-adsorption deposits (IADs) (Xu et al., 2017). This type of deposit is formed by the subtropical weathering of granitoids, followed by the absorption of REEs as ionic complexes

* Corresponding author at: Key Laboratory of Orogenic Belts and Crustal Evolution, School of Earth and Space Sciences, Peking University, Beijing 100871, China.
E-mail address: xucheng1999@pku.edu.cn (C. Xu).

https://doi.org/10.1016/j.gca.2022.12.019
0016-7037/

onto clay minerals (mostly kaolinite and halloysite) in the weathering crusts (Li et al., 2019; Borst et al., 2020).

Economically-viable HREE concentrations are predominantly sourced from the IADs in South China. These deposits primarily occur in the Jiangxi and Guangdong Provinces (Li et al., 2017, 2019). The subtropical climate facilitates deep chemical weathering and REE mobilization, accounting for approximately 80% of global HREE supplies (U.S. Geological Survey, 2022). Most granitoids in South China are enriched in LREEs, which are generally concentrated in apatite, monazite, and fluorocarbonate minerals (Li et al., 2017). Statistical analyses also show that only 3% of global granitoids are characterized by HREE enrichment relative to LREEs (8515 samples in the GEOROC database, https://georoc.eu/), and few of them form the HREE deposits. Therefore, it is imperative to access the origin of HREEs in the granitoids. The REE patterns and mineral compositions of the parent rocks impose a significant control on the formation of LREE and HREE deposits (Li et al., 2017; Xu et al., 2017). Alkaline igneous rocks typically have high REE concentrations (Linnen and Cuney, 2005; Marks and Markl, 2017) and have become a key target for REE exploration (Gysi and Williams-Jones, 2013; Estrade et al., 2019). However, nearly all HREE-rich granites in South China, which lead to economic IADs, are peraluminous (Huang et al., 1989; Sanematsu and Watanabe, 2016; Li et al., 2017). The mechanism of primary HREE enrichment in peraluminous granites remains unknown. This is a key issue in determining and assessing the origin of HREE mineralization in the IADs.

South China is famous for its large scale Mesozoic granitoid-volcanic rocks and economically significant W, Sn, U, Nb-Ta, Cu-Au, Pb-Zn-Ag, Sb, and REE mineralization (Mao et al., 2008). Most of these deposits are genetically associated with multi-stage granitoid magmatism, particularly with strongly peraluminous rocks (Zhou et al., 2006). It has long been a mystery why one area has produced large HREE mineralization. In this study, we reported data from a granitoid complex in Zudong, South China, whose weathering crusts form the largest HREE deposit worldwide. Direct mineralogical and geochemical evidence indicates an externally derived fluid-rock interaction mechanism for HREE enrichment.

2. Geological background and sampling

The South China Block (SCB) contains the Yangtze and Cathaysia sub-blocks in the north and south, respectively (Guo et al., 1989), which were amalgamated along the Jiangnan orogenic belt in the Early Neoproterozoic. The block was subsequently reworked by three tectono-thermal events in the Middle Paleozoic, Late Permian-Triassic, and Jurassic-Early Cretaceous (Hu et al., 2017; Li et al., 2017; Zhao et al., 2017). Large amounts of granites were emplaced during these events, which were attributed to flat slab subduction, tearing, and rollback of the Paleo-Pacific plate (Li and Li, 2007; Li et al., 2012). The Jurassic-Early Cretaceous granitoids are widespread in the eastern SCB and show a northeastward-younging trend toward the coast (Supplementary Material Fig. S1). These granitoids dominantly consist of biotite and muscovite granites and belong to metaluminous to peraluminous calc-alkaline I-type, alkaline A-type, strongly peraluminous S-type granites, and subordinate syenite. The A-type granites are locally associated with basalts (Zhou et al., 2006). More than 170 regolith-hosted REE deposits have been exploited in South China (Fig. S1), but only ~10% of these deposits, hosted in soils produced by granitoid weathering, are HREE dominant (Li et al., 2017).

The Zudong deposit in the eastern SCB is the largest regolith-hosted HREE deposit worldwide. Its pre-mining REE resources total 131,000 t at an average grade of 0.05 wt% of yttrium oxide, with the Y estimated to encompass 35.8 to 62.5% of the total REE resource (Xie et al., 2016). The weathering profiles at the deposit vary from a few meters to 30 m in thickness. The orebodies are predominantly preserved in the clay-rich layer. The parental granite covers an area of 32.5 km^2 along an NNE-SSW trending fault. It intruded into Early Jurassic volcanic rocks as well as Late Permian coal-bearing shale and mudstone (Fig. S1). Previous studies have classified the pluton into two types: medium- to fine-grained alkali-feldspar granite and medium- to coarse-grained biotite granite (Huang et al., 1989). The previously reported plutonic ages exhibit considerable variation. The whole-rock Rb-Sr and biotite K-Ar isochrons are 148 and 134 Ma, respectively (Huang et al., 1989). Zircon has U-Pb ages of 123.8 ± 3 Ma (Yuan and Zhang, 1992) and 168.2 ± 1.2 Ma (Zhao et al., 2014b). In this study, we identified granodiorite, biotite-muscovite alkali-feldspar granite, and muscovite alkali-feldspar granite based on typical mineral compositions. Because of hydrothermal alteration and weathering, there is no distinct border between the three rock types.

The medium-grained biotite granodiorite is composed of orthoclase (15–20 vol%), plagioclase (30–35 vol%), quartz (20–25 vol%), amphibole (10–15 vol%), and biotite (7–10 vol%). The accessory minerals include titanite, apatite, ilmenite, zircon, and monazite. Plagioclase is well-developed with platy crystals. Orthoclase and quartz have subhedral to anhedral crystals. Amphibole occurs as euhedral crystals and occasionally contains small inclusions of ilmenite (Fig. S2a). Biotite has a plate-like shape with well-developed cleavage and a straight contact boundary with feldspar and quartz. Amphiboles were locally altered by chlorite (Fig. S2b). Titanite is wedge-shaped and often coexists with amphiboles (Fig. S2b). Apatite has two occurrence types: inclusions in feldspar and quartz and long columnar crystals cutting through primary minerals (Fig. S2b). Primary monazite occurs as mineral inclusions in quartz and feldspar (Fig. 1a). The zircon has well-developed oscillatory zones and intergrows with quartz, amphibole, and titanite (Fig. 2a). The medium-grained biotite-muscovite alkali-feldspar granite is composed of orthoclase (20–25 vol%), albite (20–25 vol%), quartz (35–40 vol%), muscovite (5–7 vol%) and biotite (3–5 vol%). The accessory phases consist of rutile, apatite, zircon, fluorite, magnetite, ilmenite, columbite, and REE minerals. Orthoclase and albite crystals display irregular borders and are surrounded by quartz (Fig. S2c). Zircon crystals usually show well-developed oscillatory zones (Fig. 2b). The fine-grained muscovite alkali-feldspar granite is composed of orthoclase (20–25 vol%), albite (20–25 vol%), quartz (40–45 vol%), and muscovite (7–10 vol%). Accessory minerals include rutile, zircon, fluorite, magnetite, and REE minerals. The albite exsolves in orthoclase with joint extinction (Fig. S2f). Magmatic zircon exhibits oscillatory zones (Fig. 2c).

The two types of alkali-feldspar granites underwent strong hydrothermal metasomatism. In the biotite-muscovite granite, primary apatite was altered and contained mineral inclusions such as monazite and zircon (Fig. 1b). Hydrothermal muscovite crystallized locally at the expense of biotite (Fig. S2d) or occurred as fine-grained crystals associated with rutile, allanite, bastnäsite-(Ce), and synchysite-(Ce) in aggregates (Fig. S2e). In several cases, the aggregates appear to have a tabular, potentially monoclinic, or wedge-shaped morphology (Fig. 1c), indicating that they may be a pseudomorph of titanite. A number of monazites are associated with the altered apatite showing patchy compositional zones in cathodoluminescence (CL) images (Fig. 1b); others occur along the cleavage or crystal borders of muscovite (Fig. 1d). The HREEs are hosted by fergusonite-(Y) and synchysite-(Y), which are intergrowth with muscovite and present as anhedral crystals interstitially in quartz and feldspar (Fig. 1e). In the muscovite granite, hydrothermal zircon associated with HREE minerals contains quartz, muscovite, and feldspar inclusions (Fig. 2d). Muscovite occurs as fine-grained aggregates (Fig. S2g). The rock contains

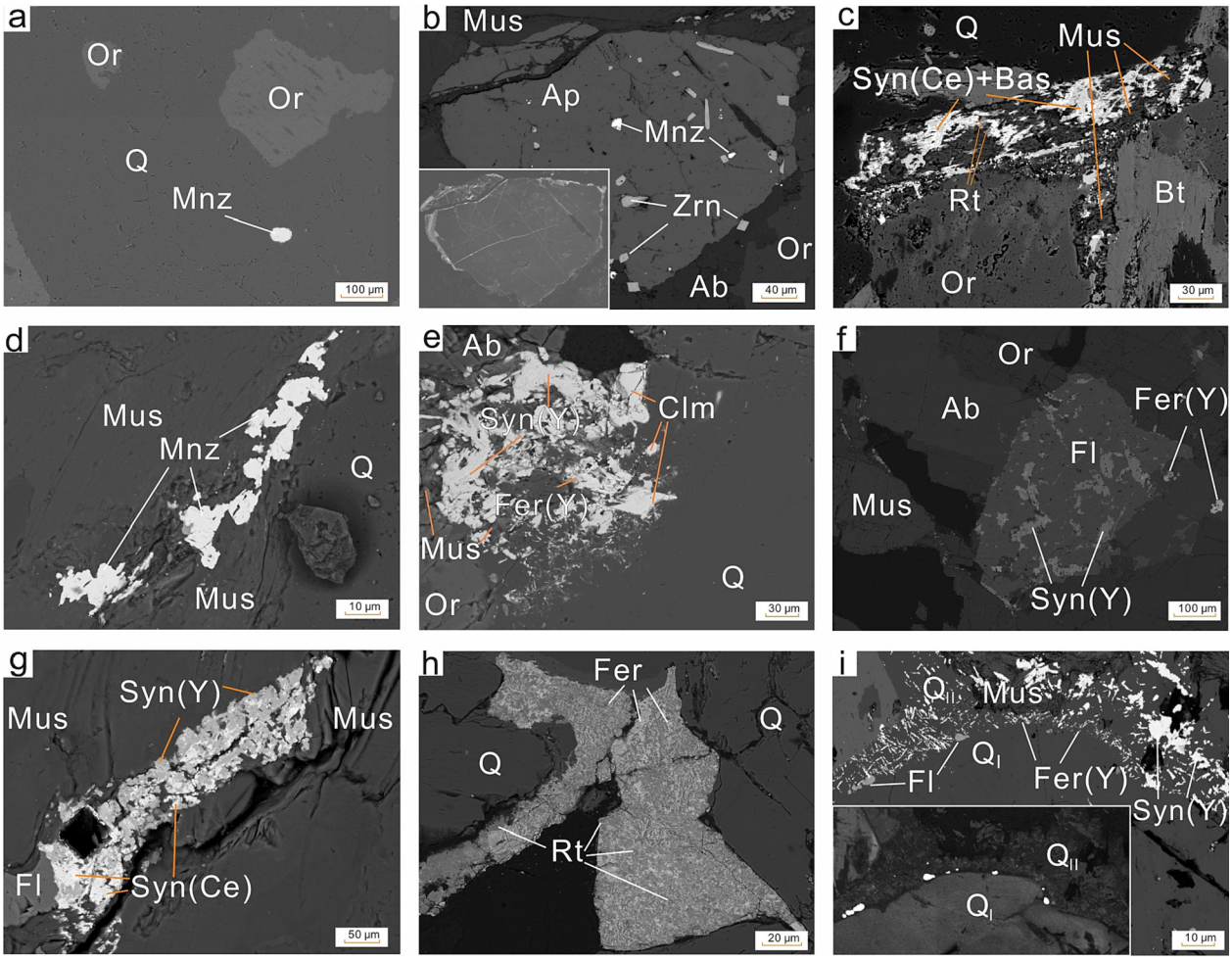

Fig. 1. Selected characteristic REE minerals in the granodiorite (a), biotite-muscovite alkali-feldspar granite (b–e) and muscovite alkali-feldspar granite (f–i) in back-scattered electron images (a–i) and CL images (b,i). Q, quartz; Or, orthoclase; Mnz, monazite; Ab, albite; Ap, apatite; Bt, biotite; Mus, muscovite; Rt, rutile; Bas, bastnäsite-(Ce); Syn(Ce), synchysite-(Ce); Fer(Y), fergusonite-(Y); Syn(Y), synchysite-(Y); Clm, columbite; Fl, fluorite.

fewer LREE minerals and more HREE minerals than biotite-muscovite granite. Hydrothermal fluorite is present as veinlet-filling fractures within feldspar (Fig. S2h). Synchysite-(Y) occurs as mineral inclusions in the fluorite (Fig. 1f). It is also associated with synchysite-(Ce) and present as disseminated anhedral grains developed within muscovite fractures (Fig. 1g). Acicular fergusonite-(Y) is intergrowth with rutile at the edge of quartz (Fig. 1h). Both the synchysite-(Y) and fergusonite-(Y) occur as overgrowths completely mantling the edges of euhedral quartz crystals (Fig. 1i). Two generations (quartz I and II) could be distinguished by CL imaging (Fig. 1i). Quartz I predates HREE minerals and has light CL. Quartz II displays growth zonation in dark CL and completely encloses synchysite-(Y) and fergusonite-(Y) inclusions, which form arrays along the boundary between growth zones.

3. Analytical methods

3.1. Rock mapping

Representative polished thin sections of granitoid samples were analyzed at Peking University, China, using a TESCAN Integrated Mineral Analyzer (TIMA) system (TESCAN, Brno, Czechia). The machine consists of a TESCAN Mira Schottky field emission scanning electron microscope with four silicon drift energy dispersive detectors. The measurements were conducted in a dot-mapping mode. To identify individual particles and the borders between several preparatory phases, back-scattered electron images were acquired. The X-ray spectra were used to generate a rectangular mesh of the observations for each phase. Spectroscopic data were compared to mineral definition files to enable mineral identification and mapping. All mineral phase volumes and mass ratios were determined automatically. The measurements were performed at a voltage of 25 kV, a field size of 1500 μm, and a working distance of 15 mm. The spot size was around 50 nm.

3.2. Mineral compositions

The major element abundances of the representative minerals in the granites were analyzed by wavelength-dispersive X-ray spectrometry (WDS) using a JEOL JXA-iHP200F (JEOL Ltd., Tokyo, Japan) electron microprobe (EMP) at the Institute of Mineral Resources, Chinese Academy of Geological Sciences. Based on the chemical composition and grain size of individual minerals, these were analyzed using a set of relevant matrix-specific standards (both natural and synthetic) and optimized machine conditions (beam settings, detector type, and counting statistics). The standards used for the WDS analyses included sanidine (Si, K), wollastonite (Ca), rutile (Ti), hematite (Fe), rhodonite (Mn), fluorite (F),

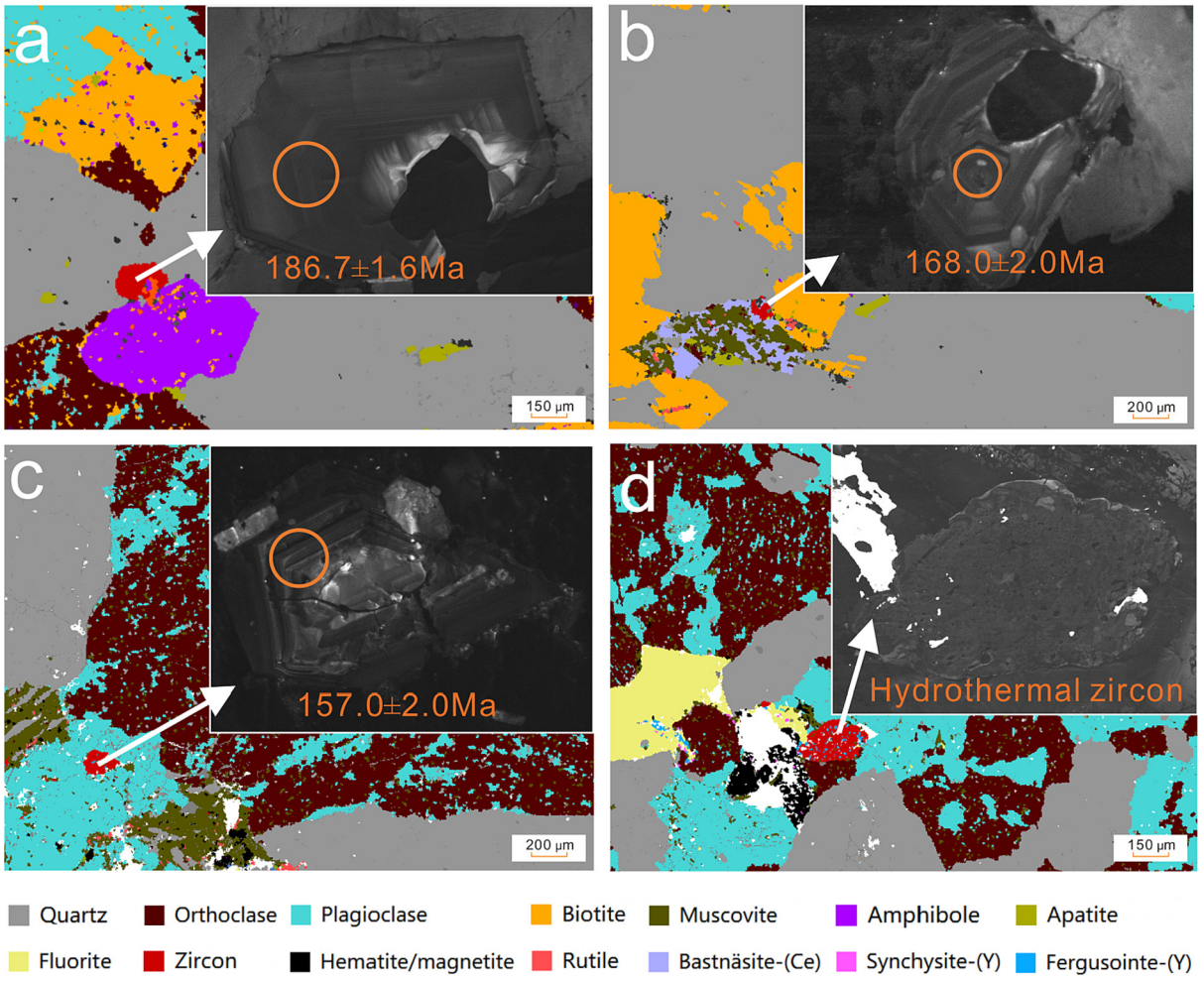

Fig. 2. Selected characteristic zircons in the granodiorite (a), biotite-muscovite granite (b), and muscovite granite (c-d) in CL images with TIMA phase maps.

jadeite (Na, Al), apatite (P), forsterite (Mg), metallic Nb, Ta, and Sc (Nb, Ta, Sc), uraninite (Th, U, Pb), NaCl (Cl) and synthetic REE phosphates. The measurements were carried out at a beam current of 20 nA and the accelerating voltage of 15 kV with the electron beam ranging 1–5 μm in diameter. Raw WDS data of REE-bearing minerals were corrected using empirical interference values for REEs and other elements that potentially interfere with the REE signals, as determined from well-characterized synthetic phosphate standards. A standard ZAF correction procedure was used to correct all raw data. The precision of the WDS analyses was ±2% or greater for most elements.

The trace element compositions of the representative silicate minerals and apatite were determined *in situ* by laser ablation inductively-coupled-plasma mass spectrometry (LA-ICP-MS) at Peking University. The machine consists of an Agilent 7500Ce mass spectrometer and a 193 nm ArF excimer laser (Agilent Technologies, Santa Clara, CA, USA). The ablation spot was 44 μm in diameter. The analyses were carried out using a laser energy density of 5.5 J/cm^2 and a repetition rate of 5 Hz. Calibration was performed using the glass standards NIST 610, 612, and 614. Silicon and calcium were selected as internal standards for silicate minerals and apatite, respectively. The SiO_2 and CaO contents of the samples, which were determined through EMP analyses, were used as the calibration standards for the ^{43}Ca and ^{29}Si data obtained by LA-ICP-MS. Repeated measurements of the glass standards indicated that the analytical error was within 5% (2σ).

3.3. Zircon U-Th-Pb geochronology

Zircon crystals were identified in polished thin sections of the rock samples using TIMA. CL imaging was used to examine the crystals and show their internal structures. A multiple collectors (MC)-ICP-MS was used to measure the zircon U and Pb isotope ratios *in situ* at Peking University. The analysis was carried out using an Agilent 7700x mass spectrometer connected to a 193 nm ArF excimer laser. With a fluency of 10 J/cm^2 and a spot measuring 32 μm in diameter, the laser beam was focused on the sample for 40 s at a repetition rate of 5 Hz. GJ-1 and Plesovice standards were used for quality control. To correct the machine mass bias and elemental fractionation, the Nancy 91500 standard was utilized as an external calibration reference. For common Pb correction, the Pb isotope composition of the present-day crust was used (Stacey and Kramers, 1975).

3.4. Zircon Hf isotope analysis

The Hf isotope ratios of zircons were analyzed using a MC-ICP-MS (Neptune Plus, Thermo Fisher Scientific, Waltham, MA, USA) at the National Research Center of Geoanalysis, Beijing. The instrument was coupled with a femtosecond (λ = 343 nm) laser ablation system (J-200). Raster mode was used to ablate the samples, with an influence of ~1 J·cm^{-2}, a repetition rate of 8 Hz, and the resulting craters of ~40 × 20 μm. The ion intensities of ^{172}Yb, ^{173}Yb,

^{175}Lu, ^{176}Hf (^{176}Yb and ^{176}Lu), ^{177}Hf, ^{178}Hf, ^{179}Hf, and ^{180}Hf were determined using the static Faraday cup mode. During this analysis, precise isobaric interference corrections for ^{176}Lu and ^{176}Yb on ^{176}Hf were determined. The isobaric interference of ^{176}Lu on ^{176}Hf was corrected by measuring the intensity of the interference-free ^{175}Lu and using the recommended ^{176}Lu/^{175}Lu value of 0.02655 (Machado and Simonetti, 2001). The ^{176}Yb/^{172}Yb value of 0.5887 and the mean mass bias of Yb (β_{Yb}) obtained on the same spot were applied for the interference correction of ^{176}Yb on ^{176}Hf (Wu et al., 2006). Standards 91500 and Plesovice were also analyzed to assess the reliability of analytical data, with weighted mean ^{176}Hf/^{177}Hf ratios of 0.282297 ± 23 (2σ) and 0.282473 ± 21 (2σ), respectively. These results were within the error of the reported values of 0.282308 ± 6 (2σ) and 0.282482 ± 13 (2σ) for these standards (Blichert-Toft, 2008; Sláma et al., 2008).

3.5. Whole-rock chemical analyses

The major and trace element compositions of the granitoid samples were determined by X-ray fluorescence spectrometry using a Shimadzu XRF-1800 instrument and solution ICP-MS using an Agilent 7500 mass spectrometer, respectively, at Beijing GeoAnalysis Laboratory Co. Ltd., China. Details of the analytical method for trace elements have been given by Liang et al. (2000). The accuracy of trace element determinations was better than 10% according to the replicate measurements (using well-characterized standards).

3.6. Nd isotope analyses

Neodymium isotopic compositions of granitoid samples were analyzed by MC-ICP-MS on the Nu Plasma II platform (Nu Instruments Ltd., Wrexham, UK) at Beijing GeoAnalysis Laboratory Co. Ltd., China. The mass fractionation corrections for Nd isotopic ratios were normalized to ^{146}Nd/^{144}Nd = 0.7219. Repeated measurements of the USGS Nd standards BHVO-2 and BCR-2 yielded ^{143}Nd/^{144}Nd ratios of 0.512991 ± 4 (2σ) and 0.512634 ± 4 (2σ), respectively. The results were within the errors of the reported values, i.e., 0.512990 ± 10 (BHVO-2) and 0.512638 ± 15 (BCR-2) (Weis et al., 2006).

The Nd isotopic compositions of REE minerals and apatite were measured *in situ* by MC-ICP-MS with a 193 nm laser ablation system (RESOlution LR, Applied Spectra, Inc., Freemont, CA, USA; and Nu Plasma II) at Nanjing FocuMS Technology Co. Ltd., China. The laser beam was focused on the sample at a fluency of 4.5 J/cm^2. Each acquisition incorporated a 20 s background, followed by a spot diameter of 23 μm at a 5 Hz repetition rate for 40 s. Integration time was set to 0.3 s (equating to 133 cycles during the 40 s period). Standard monazite (Namaqualand-2, M2, M4, and Trebilcock) and apatite (PA1, AP2) were used as quality controls for every ten analytical samples, yielding weighted mean ^{143}Nd/^{144}Nd ratios of 0.511228 ± 31 (σ), 0.511082 ± 24 (σ), 0.511082 ± 8 (σ), 0.512207 ± 21 (σ), 0.511331 ± 23 (σ), and 0.510995 ± 19 (σ). These results are within the range of reported values: 0.511225 ± 32 (Namaqualand-2), 0.511083 ± 28 (M2), 0.511087 ± 29 (M4), 0.512224 ± 30 (Trebilcock), 0.511352 ± 24 (AP1), and 0.510985 ± 16 (AP2) (Yang et al., 2014; Xu et al., 2018). ^{147}Sm/^{144}Nd elemental fractionation was calibrated against the homogeneous standard Namaqualand-2 (^{147}Sm/^{144}Nd = 0.0980 ± 3; Liu et al., 2012).

4. Results

The zircon U-Pb-Hf isotope data, major and trace elements, and Nd isotope compositions of the whole-rocks and their minerals are listed in Supplementary Material Tables S1–S7.

4.1. Zircon U-Pb geochronology and Hf isotope geochemistry

Forty-seven zircon grains in polished thin sections from the three types of granitoids were analyzed for U-Pb geochronology. Their CL images reveal clear oscillatory zonings (Fig. 2a–c), typical of magmatic origin. In the granodiorite, zircons have variable Th (621–11510 ppm) and U (1349–10520 ppm) contents and Th/U ratios of 0.2–1.4 (Table S1). The ^{206}Pb/^{238}U ages range from 183 to 195 Ma, with a peak age of 191 Ma. The biotite-muscovite granite zircons contain wide-ranged Th (645–5360 ppm) and U (1346–13440 ppm) contents, with Th/U ratios of 0.18–1.08. Their ^{206}Pb/^{238}U ages vary from 164 to 186 Ma, with a peak age of 169 Ma, which matches the previously published zircon age of 168.2 ± 1.2 Ma (Zhao et al., 2014a). In contrast, zircons in the muscovite granite have Th (1676–9740 ppm) and U (2608–24240 ppm) contents with Th/U ratios ranging from 0.38 to 1.27. They have the youngest ^{206}Pb/^{238}U ages of 149–165 Ma, with a peak age of 154 Ma (Fig. 3).

The Hf isotopic compositions of magmatic zircons from the granodiorite show consistently high $\varepsilon Hf_{(t)}$ values (5.1–8.3), similar to that from the biotite-muscovite [$\varepsilon Hf_{(t)}$ = 3.6–8.6] and muscovite alkali-feldspar granites [$\varepsilon Hf_{(t)}$ = 3.4–6.5] (Table S2).

4.2. Mineral chemistry

4.2.1. Feldspar

Fresh feldspars from the three types of granitoids were analyzed using an EMP and LA-ICP-MS (Tables S3–S4). Feldspars are classified as K-feldspar and plagioclase. Their compositional variation of feldspars can be adequately characterized in terms of three end-members: $KAlSi_3O_8$ (orthoclase, Or), $NaAlSi_3O_8$ (albite, Ab), and $CaAl_2Si_2O_8$ (anorthite, An). In the granodiorite, K-feldspar is represented by $Ab_{2.5}An_0Or_{97.4}$ to $Ab_{6.7}An_0Or_{93.2}$ and contains Al_2O_3 (~18 wt%), K_2O (~17 wt%), and trace amounts of Na_2O (up to 0.78 wt%) (Table S3). The granodiorite plagioclase corresponds to oligoclase with $Ab_{68}An_{29.1}Or_{2.7}$ to $Ab_{77}An_{21}Or_{0.8}$ and high Al_2O_3 (~23 wt%), Na_2O (~7 wt%), and CaO (~5 wt%) contents. In the biotite-muscovite granite, K-feldspar ranges from $Ab_{2.6}An_0Or_{97.4}$ to $Ab_{4.5}An_0Or_{95.5}$. The albite composition ranges from $Ab_{96}An_{3.3}Or_{0.7}$ to $Ab_{99.8}An_0Or_{0.2}$. It contains high amounts of Al_2O_3 (~20 wt%), Na_2O (~10 wt%), and trace amounts of CaO (~1.8 wt %). In the muscovite granite, K-feldspar is represented by $Ab_{2.1}An_{0.1}Or_{97.8}$ to $Ab_{8.4}An_{0.1}Or_{91.5}$. Albite ranges from $Ab_{90.1}An_{8.8}Or_{1.1}$ to $Ab_{96.1}An_3Or_{0.9}$. It has similar Al_2O_3 (~19 wt%) and Na_2O (~10 wt%) contents, and lower CaO (up to 0.6 wt%) contents than that in the biotite-muscovite granite.

All of the feldspars exhibit variable Th/U ratios (0.49–12.61 and 0.31–7.59 for plagioclase and K-feldspar, respectively). They have positive U, Pb, Sm, and Eu and negative Nb, Zr, and Ti anomalies on the primary mantle value-normalized diagram (Fig. 4a). In contrast, K-feldspar in the biotite-muscovite granite has the highest Rb/Sr ratios (~814), whereas that in the granodiorite and muscovite granite shows relatively low Rb/Sr ratios (~36 and ~2). The granodiorite feldspar has the highest Sr content (131–373 ppm; Table S4). Only trace amounts of REEs were detected in the mineral (total REE contents reaching 30.6 ppm and 18.2 ppm for plagioclase and K-feldspar, respectively). The granodiorite feldspars display strong enrichment in LREEs [$(La/Yb)_{cn} \approx 168$ and 40 for plagioclase and K-feldspar, respectively]. Positive Eu ($Eu/Eu^* = 17–64$) and negative Y anomalies were observed in this mineral (Fig. 4b). In the biotite-muscovite granite, plagioclase is characterized by higher HREE enrichment [$(La/Yb)_{cn} \approx 0.2$] and negligible Eu and negative Y anomalies. K-feldspar has low HREE abundance [$(La/Yb)_{cn} \approx 19$] and positive Eu ($Eu/Eu^* \approx 21$) anomalies. A similar REE fractional distribution was determined in feldspar from the muscovite granite. It's

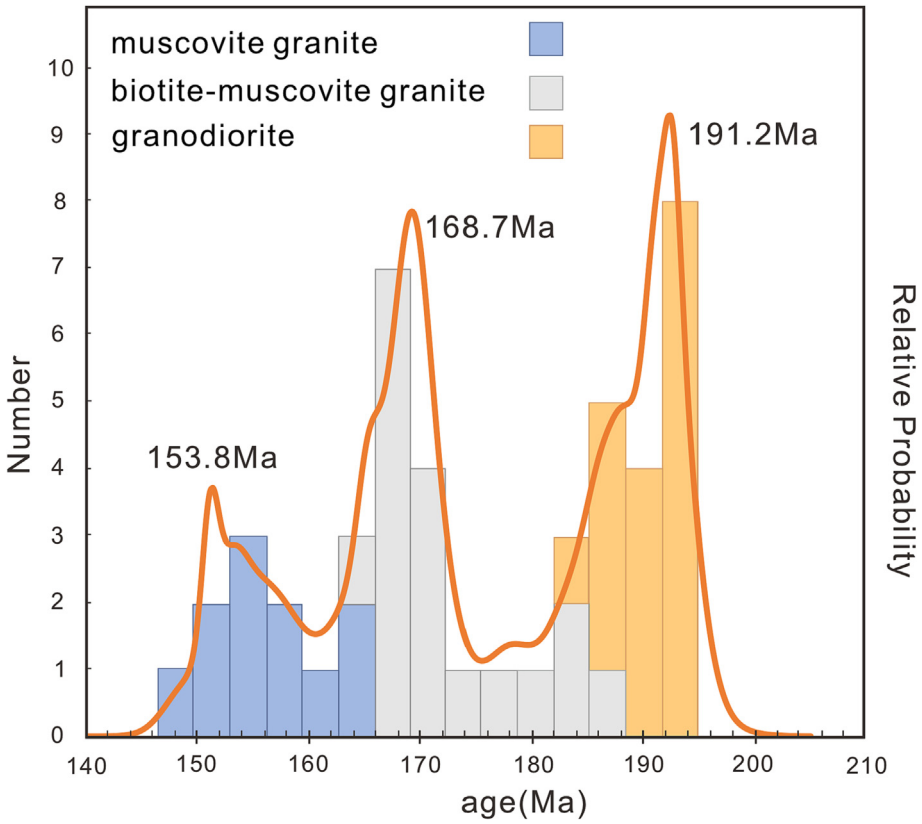

Fig. 3. Zircon U-Pb age charts of the Zudong granitoids.

K-feldspar contains low REE contents, especially HREEs, and has high REE fractionation with $(La/Yb)_{cn} \approx 7.5$ and negligible Eu and Y anomalies. Albite displays a higher REE composition and stronger HREE enrichment, with $(La/Yb)_{cn} \approx 1.2$, and is characterized by a negative Eu anomaly (Fig. 4b).

4.2.2. Mica

The granodiorite mica has Fe/(Mg + Fe) ratios ranging from 0.92 to 0.97, corresponding to annite. The mineral contains FeO (~38 wt %), K_2O (~9 wt%), TiO_2 (~2 wt%), and low MgO contents (up to 0.7 wt%). It has negative Ta, Sr, and Zr, and positive Nb anomalies, as shown in Fig. 4c. The chondrite-normalized REE pattern of the biotite displays LREE enrichment [$(La/Yb)_{cn}$ = 30–49] with negative Eu ($Eu/Eu^* \approx 0.3$) and Ce ($Ce/Ce^* \approx 0.2$) anomalies (Fig. 4d). The biotite in the biotite-muscovite granite is chemically similar to that in the granodiorite.

The muscovite in the biotite-muscovite and muscovite granites contains similar K_2O (~8.6 wt% vs ~8.7 wt%), MgO (~1.2 wt% vs ~2 wt%), and FeO (~3.7 wt% vs ~2.6 wt%) contents. Compared to the primary mantle values, the mineral is relatively depleted in Ba, Sr, and Zr and enriched in Pb, U, and Ta (Fig. 4c). It contains strong HREE enrichment with $(La/Yb)_{cn}$ of 0.04–0.62 and 0.03–0.07 in the two types of rocks, distinguishing it from biotite in the granodiorite. A negative Eu anomaly was observed in the muscovite (Fig. 4d).

4.2.3. Amphibole

Amphibole is common in granodiorite and contains small ilmenite inclusions. The mineral is characterized by FeO (~21 wt%), CaO (~11 wt%), MgO (~8 wt%), Al_2O_3 (~7 wt%), and trace TiO_2 (up to 1.46 wt%) and Na_2O (up to 1.48 wt%) contents (Table S3). Based on the amphibole-group nomenclature (Leake et al., 1997), the Fe-rich composition of the mineral, with $Fe_B < 1$ and $(Ca + Na)_B > 1$, reveals it corresponded to ferrohornblende. The mineral exhibits negative Sr, Ba, Pb, and Zr anomalies (Fig. 4e). It is slightly enriched in LREEs [$(La/Yb)_{cn}$ = 2.7–3.3] and has a negative Eu anomaly (Eu/Eu^* = 0.30–0.35; Fig. 4f).

4.2.4. Titanite

Titanite primarily occurs as euhedral crystals in the granodiorite. It contains minor Al_2O_3 (~1.4 wt%) and FeO (~1.3 wt%) contents. The mineral shows negative Sr, Ba, Pb, and positive Zr anomalies (Fig. 4e). It has high REE contents (total REEs ~1720 ppm; Table S4) and slightly flat distribution patterns [$(La/Yb)_{cn}$ = 1.5–1.9] with a negative Eu anomaly (Eu/Eu^* = 0.31–0.35; Fig. 4f).

4.2.5. Apatite

Apatite was observed in the granodiorite and biotite-muscovite granite. It is consistently enriched in F, corresponding to fluorapatite. The mineral occurs as isolated grains in the granodiorite. It has a high level of F (~2.3 wt%) and detectable Cl contents (~0.3 wt%), with positive Th and U, and negative Sr, Ti, and Ba anomalies compared to the primary mantle values (Fig. 4e). The apatite contains high REE contents (total REE compositions of ~13,000 ppm) and strong LREE enrichment [$(La/Yb)_{cn} \approx 20$]. A negative Eu anomaly ($Eu/Eu^* \approx 0.21$) was also observed (Fig. 4f). In the biotite-muscovite granite, fluorapatite is characterized by hydrothermal alteration. The mineral has a higher level of F (~3.5 wt%) than the primary phase in the granodiorite (Table S3), with positive Th and U and negative Sr, Ti, and Ba anomalies (Fig. 4e). Compared to the primary apatite in the granodiorite, a lower LREE content, higher HREE concentration [$(La/Yb)_{cn} \approx 1.2$], and stronger negative Eu anomaly ($Eu/Eu^* \approx 0.11$) were observed in the metasomatic apatite (Fig. 4f).

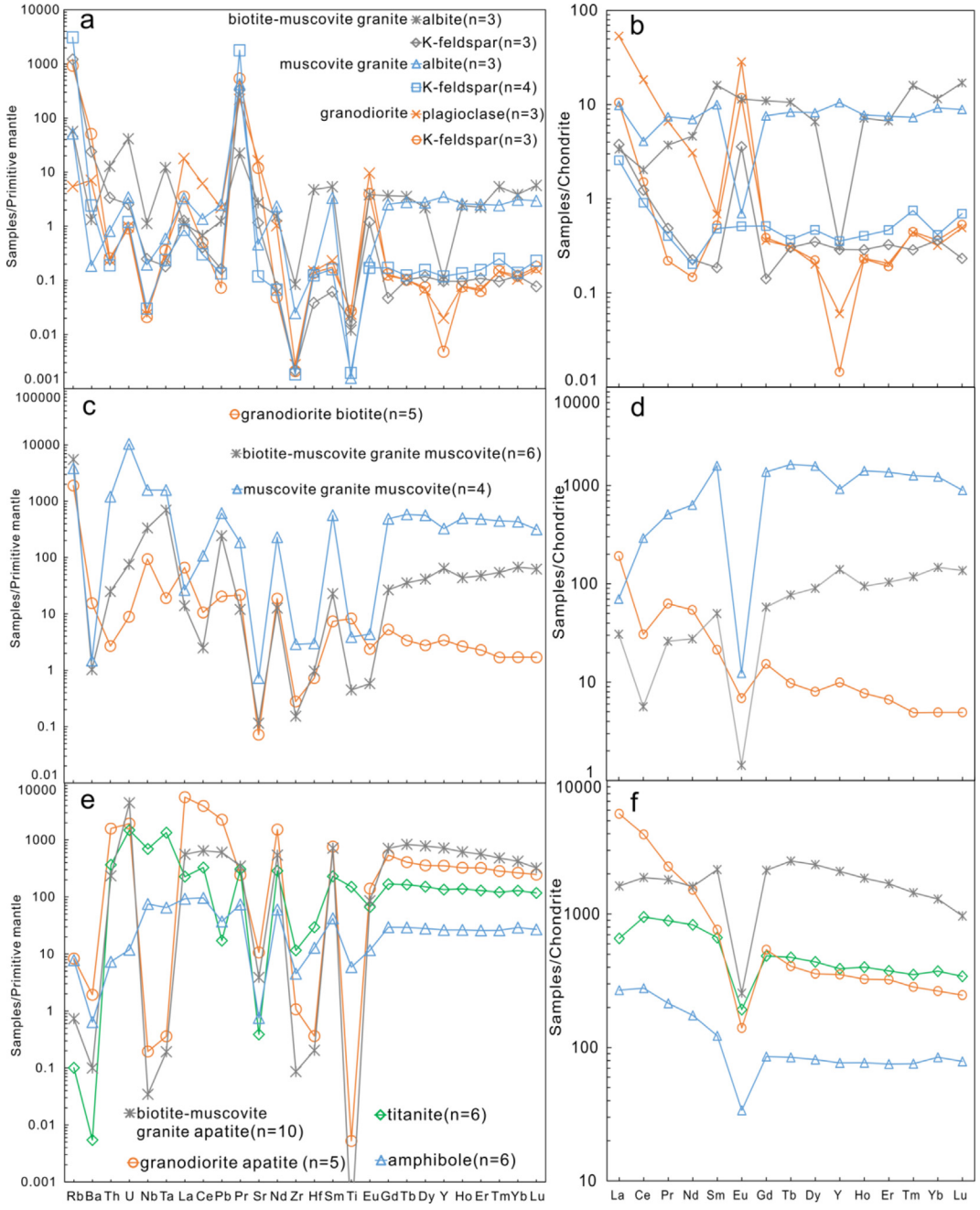

Fig. 4. Primitive mantle-normalized trace element compositions and chondrite-normalized REE distribution patterns for the representative minerals in the three types of granitoids. The values for the primitive mantle and chondrite are from Mcdonough and Sun (1995).

4.2.6. REE minerals

Monazite is an early crystallizing mineral in the granodiorite that occurs as ovoid grains wrapped by quartz or feldspar. This mineral contains Ce as the dominant lanthanide (~32 wt% oxide) and has consistently low Ca, Th, and Si contents (≤0.1, 0.1, and 0.3 wt%; Table S3). In the biotite-muscovite granite, monazite occurs as anhedral crystals associated with fluorapatite. Except for slightly higher Si and Th contents, it is chemically similar to that in the granodiorite. Bastnäsite-(Ce) is associated with synchysite-(Ce) and occurs as irregular grains. WDS analyses show that synchysite-(Ce) has a higher Y_2O_3 content (on average, 2.5 wt %) than bastnäsite-(Ce) (0.1 wt%). Synchysite-(Y) is a hydrous REE fluorocarbonate associated with fluorite and quartz. The mineral contains Y_2O_3 (~25 wt%) and CaO (~20 wt%) as dominant contents and is depleted in Eu below the detection limit (Table S3). Fergusonite-(Y) occurs with quartz and columbite and has high Y contents (~18.6 wt%) and strong depletion in Eu below the detection limit. It shows variable Si (0.01–16.3 wt%), Nb (14.9–44.8 wt %), Ta (1.3–7.5 wt%), and Ti (0.6–30.3 wt%) contents (Table S3). In the muscovite granite, synchysite-(Ce) occurs as anhedral crystals associated with fluorite. This variety is characterized by slightly lower La_2O_3 (~7.3 vs ~9.4 wt%) and Ce_2O_3 (~18 vs ~25 wt%), but higher Nd_2O_3 (~11 vs ~8.2 wt%), Sm_2O_3 (~3.8 vs ~1.7 wt%), and Gd_2O_3 (~2.5 vs ~1.7 wt%) contents relative to that of the biotite-muscovite granite (Table S3). The rock contains abundant synchysite-(Y) and fergusonite-(Y). Except for the slightly higher F (~6.3 vs ~5.7 wt%) in synchysite-(Y), they are chemically similar to those in the biotite-muscovite granite (Table S3).

4.3. Nd isotope geochemistry

Because of the high Rb/Sr ratios, the Sr isotopes of the three granitoid types were not well separated. They have different whole-rock Nd isotopic compositions. The granodiorite is characterized by the lowest $\varepsilon Nd_{(t)}$ values (−11.9 to −10.9), while the biotite-muscovite granite exhibits the highest ratios [$\varepsilon Nd_{(t)}$ = −1.6 to −1.2]. The muscovite granite initial $^{143}Nd/^{144}Nd$ ratios [$\varepsilon Nd_{(t)}$ =- −7.9 to −7.2] differ from those of the other two rock types (Table S5). The REE-rich minerals were analyzed *in situ*. The granodiorite fluorapatite and monazite contain $\varepsilon Nd_{(t)}$ values ranging from −13.8 to −10.5 and −13.0 to −11.2, respectively (Table S6). In contrast, fluorapatite and monazite-(Ce) in the biotite-muscovite granite have higher $\varepsilon Nd_{(t)}$ values (−2.5 to 2.9 and −1.1 to −0.8, respectively), similar to bastnäsite-(Ce) (−3.5 to −0.1) and fergusonite-(Y) (−3.7 to 3.0). In the muscovite granite, both LREE and HREE minerals show similar Nd isotope values [$\varepsilon Nd_{(t)}$ = −9.0 to −7.1, −10.1 to −7.8, and −11.4 to −10.3 for bastnäsite-(Ce), synchysite-(Y), and fergusonite-(Y), respectively; Table S6].

4.4. Whole-rock geochemistry

The three types of rocks display a metaluminous to peraluminous character in A/NK vs A/CNK (Fig. 5). The granodiorite contains the lowest SiO_2 (~70 wt%) and highest P_2O_5 contents (~0.2 wt%). The biotite-muscovite granite has the lowest Al_2O_3 contents (~12 wt%) and similar CaO and Na_2O abundances to the muscovite granites (Table S7). They exhibit different evolution trends in the Harker diagrams (Fig. 6). All samples are enriched in most trace elements compared to the primitive mantle, except for Sr and Ti (Fig. 7). These granites have negative Ba, Nb, Sr, and Ti, and positive Th, U, and Pb anomalies. In contrast, muscovite granite is characterized by the lowest Ba and Sr abundances (Fig. 7). The three types of rocks contain different REE compositions and patterns. The granodiorite has the lowest total REE content, and its chondrite-normalized REE pattern has a negative slope [$(La/Yb)_{cn}$ = 14–18] and Eu anomaly ($Eu/Eu^* \approx 0.2$). The biotite-muscovite granite is characterized by variable REE patterns, from LREE enrichment to slight fractionation with $(La/Yb)_{cn}$ = 2.3–8.5. The negative Eu anomaly varies from 0.01 to 0.18. The muscovite granite has the highest total REE abundance (~402 ppm), with a strong HREE enrichment pattern [$(La/Yb)_{cn}$ = 0.23–0.43] and negative Eu anomaly ($Eu/Eu^* \approx 0.01$) (Fig. 8a).

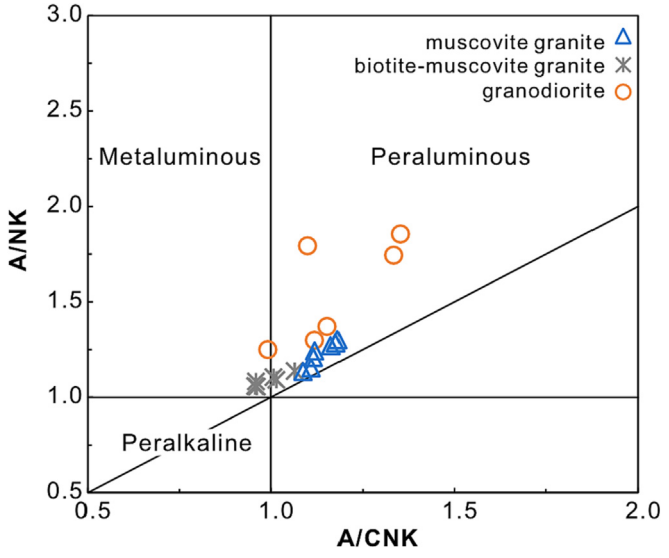

Fig. 5. A/NK vs A/CNK [A/CNK = molar ratios of $Al_2O_3/(CaO + Na_2O + K_2O)$] discrimination diagrams for the three types of granitoids. Compositional fields are from Whalen et al. (1987).

5. Discussion

5.1. Petrogenesis of the granitoid complex

REEs are generally concentrated in alkaline granites because high alkali and volatile contents can increase the solubility of REEs in the melt (Frost and Frost, 2011; Bernard et al., 2020). Recent experiments have provided evidence that alkali-rich fluids enable REEs, particularly HREEs, redistribution to form REE-rich minerals and enhance LREE and HREE mobilization at different temperatures with T ≥ 400 °C and ≤ 200 °C, respectively (Louvel et al., 2022). However, most of the HREE-rich granites in South China are peraluminous (Wu et al., 1992; Sanematsu and Watanabe, 2016). The Zudong complex, which hosts the large HREE IAD, exhibits different mineral compositions and variable REE distribution patterns. The negative Eu anomaly increasing from the granodiorite to medium-grained biotite-muscovite and fine-grained muscovite alkali-feldspar granites is likely due to fractional crystallization. However, the three types of rocks have different zircon ages and show different evolutionary trends in the plots of SiO_2 vs other major elements (Figs. 3, 6). This indicates that they are not products of fractional crystallization from the parental melts.

Biotite from the granodiorite and biotite-muscovite granite is characterized by lower MgO abundance (<0.7 wt%) than that in the adjacent Guanxi granites (~8.6 wt%; He et al., 2017). Pseudomorph of titanite, a characteristic mineral in the granodiorite, was observed in the biotite-muscovite granite (Fig. 1c). The magmatic zircons from the three types of granitoids exhibit consistent initial Hf isotope ranges [$\varepsilon Hf_{(t)}$ = 3.4 to 8.6], indicating that they have likely evolved from the same sources. However, the rocks show a large difference in their initial Nd isotope ratios (Fig. 9). The granodiorite contains the primary monazite and has strong REE fractionation. REE minerals in the biotite-muscovite and muscovite granites are metasomatic products related to hydrothermal activities, which produced muscovite, fluorite, and recrystallized quartz (Fig. 1b–f). Their initial $^{143}Nd/^{144}Nd$ ratios were similar to that of whole-rocks (Fig. 9). The secondary minerals control the Nd isotopes of the entire rock. Therefore, the Nd isotope ratios of granodiorite may reflect its source composition and is characterized by strongly low $\varepsilon Nd_{(t)}$ values (~−12), decoupled from the zircon Hf isotopes with positive $\varepsilon Hf_{(t)}$ (5.1–8.3). Anatexis of the garnet-bearing source rocks may have led to Nd-Hf isotope decoupling. Lu (HREE) was retained in the residual garnet phase, and Hf preferentially entered the melt (Schmitz et al., 2004). This also resulted in reduced HREEs in the granodiorite compared to the granitoid worldwide average (Fig. 8a).

Muscovite-bearing, peraluminous granite is generally considered an S-type rock, which was derived from metasedimentary protoliths (Barbarin, 1999; Clemens, 2003). This is not supported by our analyses, which revealed that most muscovites in the granites were formed after biotite alteration. Moreover, Al-rich garnet, a characteristic mineral in S-type granites from South China, was absent in our samples. They also have lower P abundance (Fig. 6) than typical S-type granites. Statistics and experimental data evidenced that the P concentration in I-type granites decreased with increasing SiO_2, but this trend is not recorded in S-type granites because the fractionated S-type granites are not saturated in P-bearing phases; thus, the element behaves incompatibly and increases in composition (Wolf and London, 1994; Chappell, 1999). A similar behavior was observed in South China granites

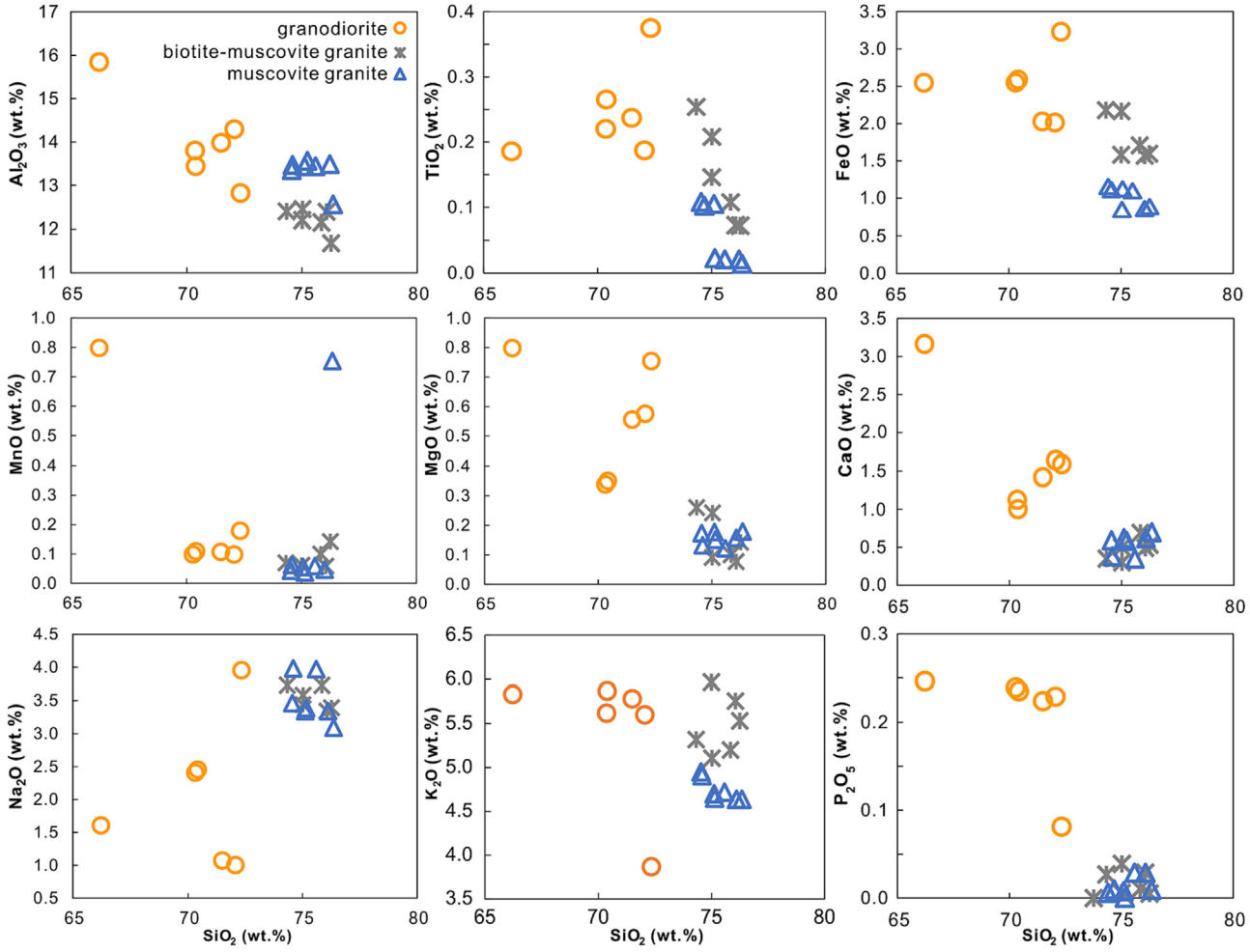

Fig. 6. Harker diagrams for the three types of granitoids.

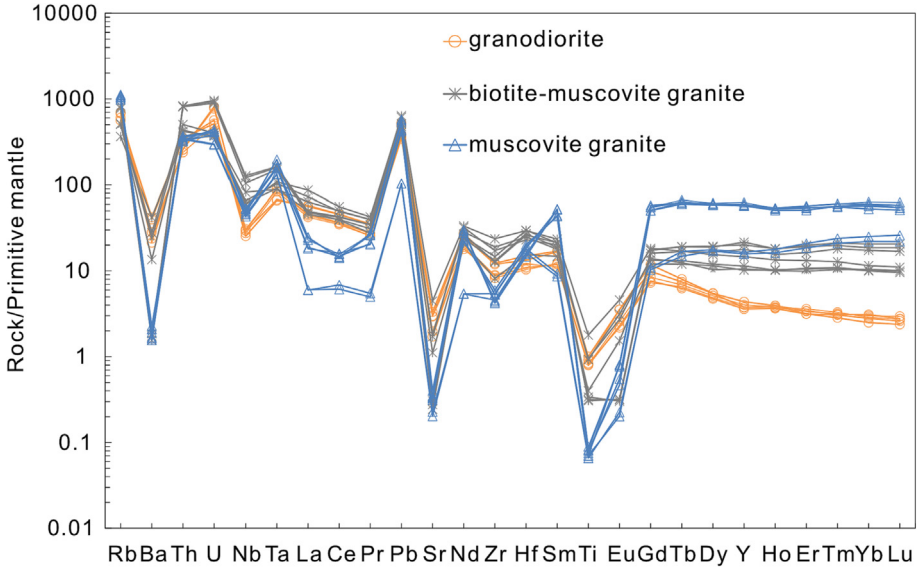

Fig. 7. Primitive mantle normalized chemical compositions for the Zudong granitoids. The primitive mantle values are from Mcdonough and Sun (1995).

(Li et al., 2007). The highly fractionated I-type granites contain lower P_2O_5 abundance (<0.05 wt%) than felsic S-type rocks (>0.1 wt%). Therefore, the biotite-muscovite and muscovite granites were derived from the same sources as the associated granodiorite. The latter has Nd model ages of 1.9–2.0 Ga, similar to the age of the basement in the study area (zircon U-Pb age of 1.87 Ga;

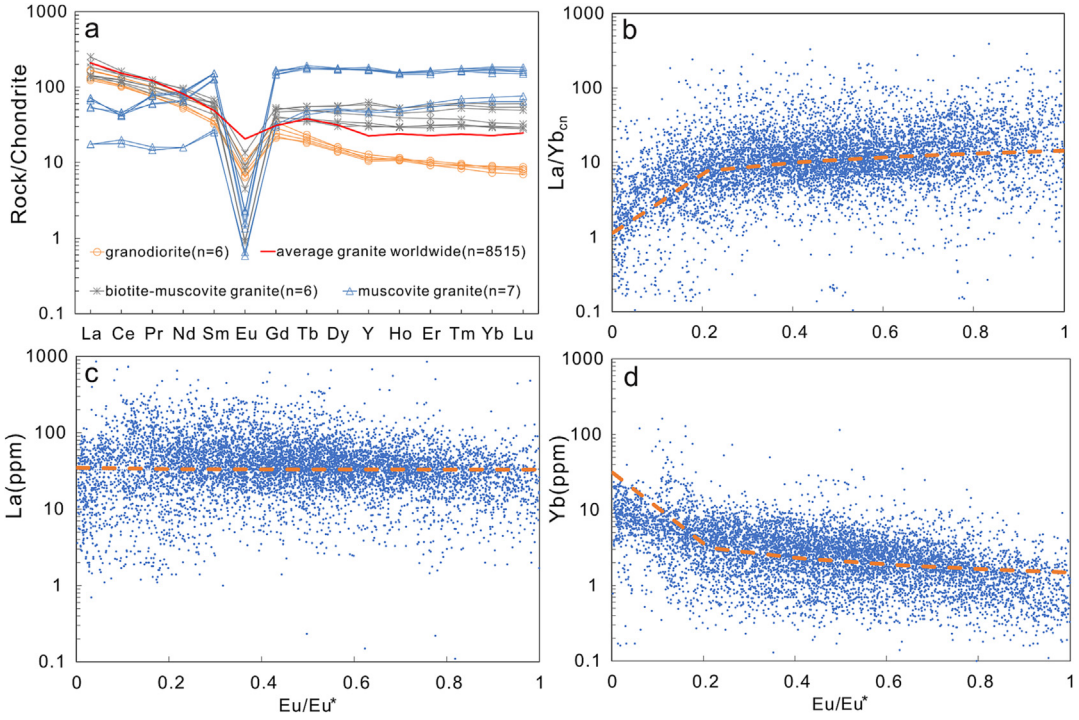

Fig. 8. Chondrite-normalized REE pattern of the Zudong granitoids (a) and REE data compilation for global granitoids (b–d). The chondrite values are from Mcdonough and Sun (1995). Data of global granitoids were downloaded from the GEOROC database (https://georoc.eu/) on March 25, 2022. The power function was used to determine the trend line in b–d.

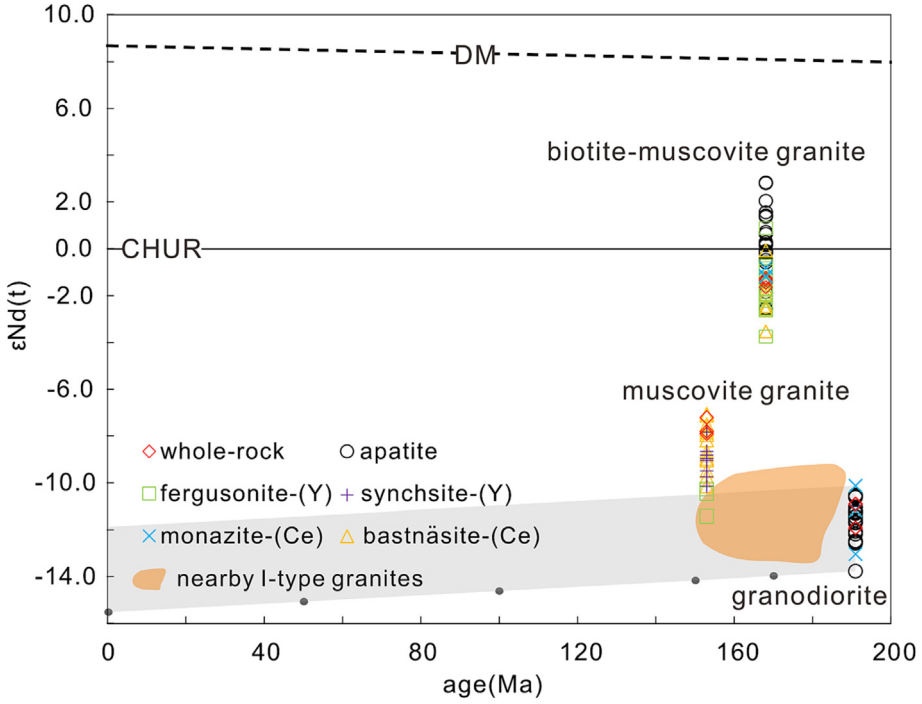

Fig. 9. $\varepsilon Nd_{(t)}$ values of REE minerals and whole rocks. The shadow shows the evolution of εNd through radiometric decay from the early granodiorite with an average $^{147}Sm/^{144}Nd$ of whole rocks at 170, 150, 100, 50 Ma, and present. CHUR, chondritic uniform reservoir; DM, depleted mantle. The shadow range of Nd isotopes is from Jurassic I-type granites in central South China (Zhang et al., 2017; Jiang et al., 2018; Wang et al., 2021).

Zhang et al., 1999). The granodiorite also exhibits similar Nd isotopic compositions to the basement-derived Jurassic-Early Cretaceous I-type granites in central South China (Fig. 9). The Paleoproterozoic basement is dominantly composed of mica, garnet-bearing schist, gneiss and amphibolite (Liu, 1997). Patiño Douce and Beard (1995) performed experiments indicating that peraluminous granodioritic and granitic magmas can be generated by the partial melting of biotite gneiss and quartz amphibolitic protoliths, respectively. Therefore, we infer that the basement compositions control the aluminum saturation features in the

granitoids. However, such garnet-containing source rocks would lead to HREE depletion in primary granitoid magmas.

5.2. HREE enrichment in peraluminous granite

The enrichment of REEs in granitoids is largely due to the magma oxidation state, fractional crystallization, and alkali-rich compositions (Chakhmouradian and Zaitsev, 2012; Marks and Markl, 2017; Watanabe et al., 2017; Bernard et al., 2020). Watanabe et al. (2017) suggested that REE-rich granitoids formed from fractionated, reduced magmas because titanite and allanite generally occurred in the oxidized granitoids, and their fractional crystallization would lead to REE depletion in residual melts. However, titanite, allanite, and magnetite are widely present in REE-rich granitoids from South China (Li et al., 2017). Cerium-poor LREE minerals, indicators of high oxygen fugacity, have also been reported in REE-rich granites from the adjacent Zhaibei area (Xu et al., 2017). Considering that feldspar is a major fractionating mineral and has a compatible partition coefficient for Eu (Bea et al., 1994), we compiled REE data vs Eu anomalies for granitoids worldwide. This provides direct geochemical evidence that there is no apparent correlation between the REE concentrations and degrees of differentiation, especially for LREEs (Fig. 8b-c). Although fractional crystallization of feldspar and quartz should enrich REEs (except for Eu), it could have led to the fractionation of early LREE-rich minerals, such as apatite and titanite. This is demonstrated by the muscovite granite, which is characterized by a stronger negative Eu anomaly and LREE depletion than both granodiorite and biotite-muscovite granite (Fig. 8a). Note that Yb (HREE) shows a sudden increase with Eu anomaly <0.2, whereas La/Yb_{cn} decreases accordingly (Fig. 8b, d). Both experimental and natural evidence suggest that peralkaline melts have high halogen solubilities (Bureau and Métrich, 2003; Giehl et al., 2014; Marks and Markl, 2017). A high concentration of volatiles in the parental magmas may add fractionated melt to the magma bodies. Sisson and Bacon (1999) suggested that gas-driven filter pressing is the dominant process for segregating highly evolved melts from the high-density crystal mush. Their significant fraction would reach volatile saturation and exsolve a low-density, viscous, halogen-rich fluid (Bachmann, 2004), which may mobilize the REEs, particularly HREEs (Migdisov et al., 2016), and metasomatized granitoids during their emplacement. However, highly fractionated peraluminous granites are generally associated with Li, W-Sn, and Nb-Ta ore deposits (Clarke, 1992; Mao et al., 2008). How HREEs arise in peraluminous granites remains unknown.

In contrast to the granodiorite, the biotite-muscovite and muscovite granites show variable REE patterns. Strong metasomatism recorded in the muscovite granites produced higher HREE concentrations and muscovite compositions. Most of the HREE minerals in both rocks occur as secondary aggregates associated with muscovite, fluorite, and late-generation quartz (Fig. 1). Metasomatic apatite in biotite-muscovite granite contains a higher HREE abundance than primary apatite in the granodiorite. High REE content, particularly for HREE composition, has been identified in the muscovite (Fig. 4). This constrains the hydrothermal fluid metasomatism as the mechanism for HREE enrichment during the emplacement of granite melts. The magmatic zircons from the three types of rocks have similar initial Hf isotopes, but the REE minerals in biotite-muscovite and muscovite granites exhibit higher initial Nd isotopic compositions than the primary phases in the granodiorite and typical I-type granites in the adjacent areas (Fig. 9), indicating the metasomatic fluids were not derived from the basement.

A key question remains regarding the origin of the metasomatic liquids, including the input of mantle sources, wall rocks, meteoric water, and recycled slab. The secondary HREE minerals in the two alkali-feldspar granites are characterized by high initial Nd isotopes. This indicates that the metasomatic fluid evolved from a relatively depleted source. Mantle-derived liquids can be eliminated as the contemporary mafic rocks (basalt and diabase) in the study area have lower $\varepsilon Nd_{(t)}$ values (−7.9 to 1.1; Wang et al., 2003; Zhang, 2004) than those of the biotite-muscovite granites and their REE-rich minerals (Fig. 9). Contamination of the wall rocks in the Permian-Triassic shale and clastic rocks ($\varepsilon Nd_{(t)}$ = −14 to −11; Shen et al., 2003) would also result in low Nd isotopes, in contrast to our data. Importantly, the above-mentioned liquids are not typically rich in REEs. Circulating meteoric water could contain high REE contents derived from the dissolution of REE minerals in the early granites during weathering, but it would inherit the low $\varepsilon Nd_{(t)}$ of the granodiorite.

Geophysical and geochemical data suggest the existence of Paleo-Pacific plate subduction beneath Mesozoic South China (Zhou and Li, 2000; Li and Li, 2007). A flat-slab subduction model was proposed to describe large-scale multi-stage magmatism in South China (Li and Li, 2007). From the Early Jurassic to Late Jurassic, the slab underwent break-off, foundering, and rollback, which triggered dehydration and partial melting of the slab. Seafloor sediments generally contain significantly high REE compositions (Kato et al., 2011). The melting of the sediment layer on the subducted slab could have produced REE- and volatile-rich liquids. Experiments have shown that ligands such as F^- and CO_3^{2-} significantly enhance REE solubility in slab-derived liquids (Tsay et al., 2014). Fluorite is associated with HREE minerals in the parental rocks (Fig. 1e–f). Moreover, different mixing proportions between the sediments and oceanic crust may have resulted in the Nd isotope variations recorded in the slab-derived liquids. This explains the difference in the initial Nd isotopic ratios of the secondary REE minerals in the biotite-muscovite and muscovite granites. As a result, an external REE- and volatile-rich liquid contribution into the granitoid magma chamber can reduce melt viscosity (Dingwell et al., 1992). This accelerates the segregation of highly

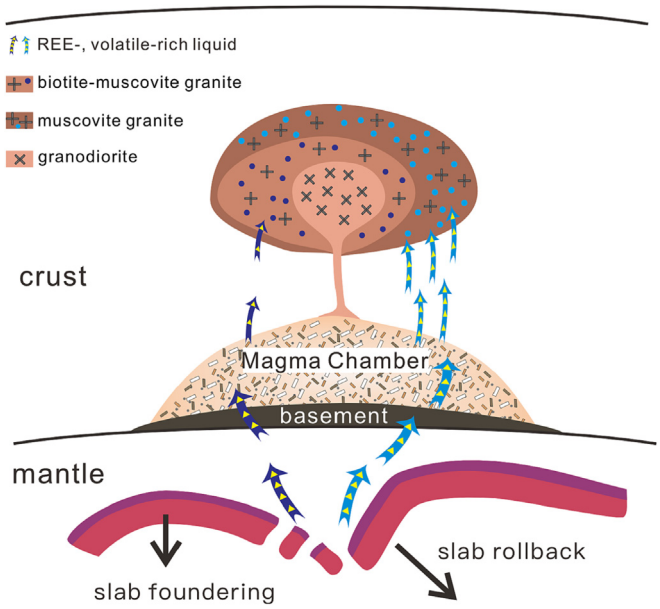

Fig. 10. Cartoon depicting the REE enrichment process for peraluminous granite. Slab-derived REE-, volatile-rich liquid contribution into the magma chamber gives rise to highly evolved melts segregating from and volatile saturation in the peraluminous parental melts. The exsolved volatile-rich fluids may transport REEs, especially HREEs, and interact with the granites during their emplacement. The subducted slab underwent break-off and foundering in the Early Jurassic and further rollback in the Middle Jurassic, triggering slab dehydration (Li and Li, 2007).

evolved melts and volatile saturation in the peraluminous parental bodies. The exsolved ligand-rich liquids may transport REEs, particularly HREEs, at relatively low-temperature conditions (Louvel et al., 2022), and interact with granites during their emplacement (Fig. 10). We infer this process has produced strong HREE enrichment in the highly fractionated peraluminous granites.

6. Conclusions

The Zudong complex in South China is composed of granodiorite, biotite-muscovite alkali-feldspar granite, and muscovite alkali-feldspar granite. These rocks have different REE patterns, from HREE depletion to enrichment relative to LREEs, with increasing negative Eu anomalies. The three types of rocks evolved from the same sources but were not products of fractional crystallization. The biotite-muscovite and muscovite granites contain abundant HREE minerals associated with late fluorite, muscovite, and quartz. The strong HREE enrichment recorded in the peraluminous granites could not be caused by fractional crystallization and source compositions but was related to external volatile- and REE-rich fluid metasomatism. The liquids may have been released from the subducted slab beneath the Mesozoic South China. In a peraluminous system, the replenishment by external fluids is crucial for the formation of highly silicic melts and HREE enrichment. The identification of HREE mineralization within the protoliths of deposits formed by weathering could be used to successfully target HREE exploration potential.

Data availability

The data are available as part of the Supplementary Material.

Declaration of Competing Interest

The authors declare that they have no known competing financial interests or personal relationships that could have appeared to influence the work reported in this paper.

Acknowledgements

This research was financially supported by the National Natural Science Foundation of China (41825008, 92162219) and Guangxi Natural Science Foundation (Guike AB22035045, 2020GXNSFGA297003). MS acknowledges support from the UKRI Natural Environment Research Council grant NE/V008935/1. J. K. was supported by the Czech Science Foundation GACR EXPRO (grant number 19-29124X). We thank Z.Y. Chen for mineral analyses, and Z. Zhao for field assistance. We are grateful to Editors Jeffrey G. Catalano, Adam Simon, and three anonymous reviewers for their constructive comments.

Appendix A. Supplementary material

Supplementary material to this article can be found online at https://doi.org/10.1016/j.gca.2022.12.019.

References

Bachmann, O., 2004. On the Origin of Crystal-poor Rhyolites: Extracted from Batholithic Crystal Mushes. J. Petrol. 45, 1565–1582.
Barbarin, B., 1999. A review of the relationships between granitoid types, their origins and their geodynamic environments. Lithos 46, 605–626.
Bea, F., Pereira, M.D., Stroh, A., 1994. Mineral/leucosome trace-element partitioning in a peraluminous migmatite (a laser ablation-ICP-MS study). Chem. Geol. 117, 291–312.
Bernard, C., Estrade, G., Salvi, S., Beziat, D., Smith, M., 2020. Alkali pyroxenes and amphiboles: a window on rare earth elements and other high field strength elements behavior through the magmatic-hydrothermal transition of peralkaline granitic systems. Contrib. Mineral. Petrol. 175, 81.
Blichert-Toft, J., 2008. The Hf isotopic composition of zircon reference material 91500. Chem. Geol. 253, 252–257.
Borst, A.M., Smith, M.P., Finch, A.A., Estrade, G., Villanova-de-Benavent, C., Nason, P., Marquis, E., Horsburgh, N.J., Goodenough, K.M., Xu, C., Kynicky, J., Geraki, K., 2020. Adsorption of rare earth elements in regolith-hosted clay deposits. Nat. Commun. 11, 4386.
Bureau, H.E., Métrich, N., 2003. An experimental study of bromine behaviour in water-saturated silicic melts. Geochim. Cosmochim. Acta 67, 1689–1697.
Chakhmouradian, A.R., Zaitsev, A.N., 2012. Rare earth mineralization in igneous rocks: Sources and processes. Elements 8, 347–353.
Chappell, B.W., 1999. Aluminium saturation in I- and S-type granites and the characterization of fractionated haplogranites. Lithos 46, 535–551.
Clarke, D.B., 1992. Granitoid Rocks. Chapman & Hall, London.
Clemens, J.D., 2003. S-type granitic magmas—petrogenetic issues, models and evidence. Earth Sci. Rev. 61, 1–18.
Dingwell, D.B., Knoche, R., Webb, S.L., Pichavant, M., 1992. The effect of B_2O_3 on the viscosity of haplogranitic liquids. Am. Mineral. 77, 457–461.
Estrade, G., Marquis, E., Smith, M., Goodenough, K., Nason, P., 2019. REE concentration processes in ion adsorption deposits: Evidence from the Ambohimirahavavy alkaline complex in Madagascar. Ore Geol. Rev. 112, 103027.
Frost, C.D., Frost, B.R., 2011. On Ferroan (A-type) granitoids: their compositional variability and modes of origin. J. Petrol. 52, 39–53.
Giehl, C., Marks, M.A.W., Nowak, M., 2014. An experimental study on the influence of fluorine and chlorine on phase relations in peralkaline phonolitic melts. Contrib. Mineral. Petrol. 167, 977.
Guo, L., Shi, Y., Lu, H., Ma, R., Dong, H., Yang, S., 1989. The Pre-Devonian tectonic patterns and evolution of South China. J. Southeast Asian Earth Sci. 3, 87–93.
Gysi, A.P., Williams-Jones, A.E., 2013. Hydrothermal mobilization of pegmatite-hosted REE and Zr at Strange Lake, Canada: A reaction path model. Geochim. Cosmochim. Acta 122, 324–352.
He, C., Xu, C., Zhao, Z., Kynicky, J., Song, W.L., Wang, L.Z., 2017. Petrogenesis and mineralization of REE-rich granites in Qingxi and Guanxi, Nanling region, South China. Ore Geol. Rev. 81, 309–325.
Hu, R.Z., Chen, W.T., Xu, D.R., Zhou, M.F., 2017. Reviews and new metallogenic models of mineral deposits in South China: An introduction. J. Asian Earth Sci. 137, 1–8.
Huang, D.H., Wu, C.Y., Han, J.Z., Zhang, Q.D., 1989. Characteristics of isotopic systematics of U-Pb and Rb-Sr and their geological implications for Zudong and Guanxi granitic intrusives, Longnan County, Jiangxi Province. Acta Geol. Sin. 1, 37–48.
Jiang, H., Jiang, S.Y., Li, W.Q., Zhao, K.D., Peng, N.J., 2018. Highly fractionated Jurassic I-type granites and related tungsten mineralization in the Shirenzhang deposit, northern Guangdong, South China: Evidence from cassiterite and zircon U-Pb ages, geochemistry and Sr-Nd-Pb-Hf isotopes. Lithos 312, 186–203.
Kato, Y., Fujinaga, K., Nakamura, K., Takaya, Y., Kitamura, K., Ohta, J., Toda, R., Nakashima, T., Iwamori, H., 2011. Deep-sea mud in the Pacific Ocean as a potential resource for rare-earth elements. Nat. Geosci. 4, 535–539.
Leake, B.E., Woolley, A.R., Arps, C.E.S., Birch, W.D., Gilbert, M.C., Grice, J.D., Hawthorne, F.C., Kato, A., Kisch, H.J., Krivovichev, V.G., Linthout, K., Laird, J., Mandarino, J.A., Maresch, W.V., Nickel, E.H., Rock, N.M.S., Schumacher, J.C., Smith, D.C., Stephenson, N.C.N., Ungaretti, L., Whittaker, E.J.W., Youzhi, G., 1997. Nomenclature of amphiboles: Report of the subcommittee on amphiboles of the international mineralogical association, commission on new minerals and mineral names. Am. Mineral. 82, 1019–1037.
Li, X.H., Li, W.X., Li, Z.X., 2007. On the genetic classification and tectonic implications of the Early Yanshanian granitoids in the Nanling Range, South China. Chin. Sci. Bull. 52, 1873–1885.
Li, Z.X., Li, X.H., 2007. Formation of the 1300-km-wide intracontinental orogen and postorogenic magmatic province in Mesozoic South China: A flat-slab subduction model. Geology 35, 179–182.
Li, Z.X., Li, X.H., Chung, S.L., Lo, C.H., Xu, X.S., Li, W.X., 2012. Magmatic switch-on and switch-off along the South China continental margin since the Permian: Transition from an Andean-type to a Western Pacific-type plate boundary. Tectonophysics 532–535, 271–290.
Li, Y.H.M., Zhao, W.W., Zhou, M.F., 2017. Nature of parent rocks, mineralization styles and ore genesis of regolith-hosted REE deposits in South China: An integrated genetic model. J. Asian Earth Sci. 148, 65–95.
Li, Y.H.M., Zhou, M.F., Williams-Jones, A.E., 2019. The genesis of regolith-hosted heavy rare earth element deposits: insights from the world-class Zudong deposit in Jiangxi Province, South China. Econ. Geol. 114, 541–568.
Liang, Q., Jing, H., Gregoire, D.C., 2000. Determination of trace elements in granites by inductively coupled plasma mass spectrometry. Talanta 51, 507–513.
Linnen, R.L., Cuney, M., 2005. Granite-related rare-element deposits and experimental constraints on Ta-Nb-W-Sn-Zr-Hf, mineralization. In: Linnen, R. L., Samson, I.M. (Eds.), Rare-element Geochemistry and Mineral Deposits,. Geological Association of Canada, GAC, Short Course, Canada.
Liu, Y.G., 1997. Stratigraphy of Jiangxi Province. China University of Geosciences Press, China.
Liu, Z.C., Wu, F.Y., Yang, Y.H., Yang, J.H., Wilde, S.A., 2012. Neodymium isotopic compositions of the standard monazites used in U-Th-Pb geochronology. Chem. Geol. 334, 221–239.
Louvel, M., Etschmann, B., Guan, Q., Testemale, D., Brugger, J., 2022. Carbonate complexation enhances hydrothermal transport of rare earth elements in alkaline fluids. Nat. Commun. 13, 1456.

Machado, N., Simonetti, A., 2001. U–Pb dating and Hf isotopic composition of zircon by laser-ablation MC–ICP–MS. In: Sylvester, P. (Ed.), Laser-Ablation–ICPMS in the Earth Sciences: Principles and Applications. Mineralogical Association of Canada, St. John's, Newfoundland, pp. 121–146.

Mao, J.W., Xie, G.Q., Guo, C.L., Yuan, S.D., Cheng, Y.B., Chen, Y.C., 2008. Spatial-temporal distribution of Mesozoic ore deposits in South China and their metallogenic settings. Geol. J. China Uni. 14, 510–526.

Marks, M.A.W., Markl, G., 2017. A global review on agpaitic rocks. Earth Sci. Rev. 173, 229–258.

Mcdonough, W.F., Sun, S.S., 1995. The composition of the Earth. Chem. Geol. 120, 223–253.

Migdisov, A., Williams-Jones, A.E., Brugger, J., Caporuscio, F.A., 2016. Hydrothermal transport, deposition, and fractionation of the REE: Experimental data and thermodynamic calculations. Chem. Geol. 439, 13–42.

Patiño Douce, A.E., Beard, J.S., 1995. Dehydration-melting of biotite gneiss and quartz amphibolite from 3 to 15 kbar. J. Petrol. 36, 707–738.

Sanematsu, K., Watanabe, Y., 2016. Characteristics and genesis of ion adsorption-type rare earth element deposits. Rev. Econ. Geol. 18, 55–79.

Schmitz, M.D., Vervoort, J.D., Bowring, S.A., Patchett, P.J., 2004. Decoupling of the Lu-Hf and Sm-Nd isotope systems during the evolution of granulitic lower crust beneath southern Africa. Geology 32, 405–408.

Shen, W., Yu, J., Zhao, L., Chen, Z., Lin, H., 2003. Nd isotopic characteristics of post-Archean sediments from the Eastern Nanling Range: Evidence for crustal evolution. Chin. Sci. Bull. 48, 1679–1685.

Simandl, G.J., 2014. Geology and market-dependent significance of rare earth element resources. Miner. Deposita 49, 889–904.

Sisson, T.W., Bacon, C.R., 1999. Gas-driven filter pressing in magmas. Geology 27, 613–616.

Sláma, J., Košler, J., Condon, D.J., Crowley, J.L., Gerdes, A., Hanchar, J.M., Horstwood, M.S.A., Morris, G.A., Nasdala, L., Norberg, N., Schaltegger, U., Schoene, B., Tubrett, M.N., Whitehouse, M.J., 2008. Plešovice zircon—A new natural reference material for U-Pb and Hf isotopic microanalysis. Chem. Geol. 249, 1–35.

Stacey, J.S., Kramers, J.D., 1975. Approximation of terrestrial lead isotope evolution by a two-stage model. Earth Planet. Sci. Lett. 26, 207–221.

Tsay, A., Zajacz, Z., Sanchez-Valle, C., 2014. Efficient mobilization and fractionation of rare-earth elements by aqueous fluids upon slab dehydration. Earth Planet. Sci. Lett. 398, 101–112.

U.S. Geological Survey, 2022. Mineral Commodity Summaries 2022. U.S. Geological Survey, Reston.

Wang, H., Feng, C.Y., Li, R.X., Zhao, C., Liu, P., Wang, G.H., Hao, Y.J., 2021. Petrogenesis of the Xingluokeng W-bearing granitic stock, western Fujian Province, SE China and its genetic link to W mineralization. Ore Geol. Rev. 132, 103987.

Wang, Y.J., Fan, W.M., Guo, F., Peng, T.P., Li, C.W., 2003. Geochemistry of Mesozoic mafic rocks adjacent to the Chenzhou-Linwu fault, South China: Implications for the lithospheric boundary between the Yangtze and Cathaysia blocks. Int. Geol. Rev. 45, 263–286.

Watanabe, Y., Kon, Y., Echigo, T., Kamei, A., 2017. Differential fractionation of rare earth elements in oxidized and reduced granitic rocks: implication for heavy rare earth enriched ion adsorption mineralization. Res. Geol. 67, 35–52.

Weis, D., Kieffer, B., Maerschalk, C., Barling, J., De Jong, J., Williams, G.A., Hanano, D., Pretorius, W., Mattielli, N., Scoates, J.S., Goolaerts, A., Friedman, R.M., Mahoney, J.B., 2006. High-precision isotopic characterization of USGS reference materials by TIMS and MC-ICP-MS. Geochem. Geophys. Geosyst. 7, Q08006.

Whalen, J.B., Currie, K.L., Chappell, B.W., 1987. A-type granites: Geochemical characteristics, discrimination and petrogenesis. Contrib. Mineral. Petrol. 95, 407–419.

Wolf, M.B., London, D., 1994. Apatite dissolution into peraluminous haplogranitic melts: An experimental study of solubilities and mechanisms. Geochim. Cosmochim. Acta 58, 4127–4145.

Wu, C.Y., Bai, G., Huang, D.H., Zhu, Z.S., 1992. Characteristics and significance of HREE-rich granitoids of the Nanling Mountain area. Bul. Chin. Acad. Geol. Sci. 25, 43–58.

Wu, F.Y., Yang, Y.H., Xie, L.W., Yang, J.H., Xu, P., 2006. Hf isotopic compositions of the standard zircons and baddeleyites used in U-Pb geochronology. Chem. Geol. 234, 105–126.

Xie, Y., Hou, Z., Goldfarb, R.J., Guo, X., Wang, L., Verplanck, P.L., Hitzman, M.W., 2016. Rare earth element deposits in China. Rev. Econ. Geol. 18, 115–136.

Xu, C., Kynicky, J., Smith, M.P., Kopriva, A., Brtnicky, M., Urubek, T., Yang, Y., Zhao, Z., He, C., Song, W., 2017. Origin of heavy rare earth mineralization in South China. Nat. Commun. 8, 14598.

Xu, L., Yang, J., Ni, Q., Yang, Y., Hu, Z., Liu, Y., Wu, Y., Luo, T., Hu, S., 2018. Determination of Sm-Nd Isotopic compositions in fifteen geological materials using laser ablation MC-ICP-MS and application to monazite geochronology of metasedimentary rock in the North China Craton. Geostand. Geoanal. Res. 42, 379–394.

Yang, Y.H., Wu, F.Y., Yang, J.H., Chew, D.M., Xie, L.W., Chu, Z.Y., Zhang, Y.B., Huang, C., 2014. Sr and Nd isotopic compositions of apatite reference materials used in U-Th–Pb geochronology. Chem. Geol. 385, 35–55.

Yuan, Z.X., Zhang, Z.Q., 1992. Sm-Nd isotopic characteristics of granitoids in the Nanling region and their petro-genetic analysis. Geol. Rev. 1, 1–15.

Zhang, S.M., 2004. Study on Nd and Sr isotopes of Yianshanian mafic rocks in East Nanling area. J. East China Uni. Tech. 27, 129–134.

Zhang, H., Sun, D., Zhu, B., 1999. The geochemical characteristics of metamorphic basic volcanics from Xingzi Group, Lushan and the tectonic implications. Acta Petrol. Sin. 15, 372–378.

Zhang, Y., Yang, J.H., Chen, J.Y., Wang, H., Xiang, Y.X., 2017. Petrogenesis of Jurassic tungsten-bearing granites in the Nanling Range, South China: Evidence from whole-rock geochemistry and zircon U-Pb and Hf-O isotopes. Lithos 278, 166–180.

Zhao, Z., Wang, D.H., Chen, Z., Guo, N., Liu, X., He, H., 2014a. Metallogenic specialization of rare earth mineralized igneous rocks in the eastern Nanling region. Geotectonica et Metallogenia 38, 255–263.

Zhao, Z., Wang, D.H., Chen, Z.Y., Chen, Z.H., Liu, X.X., 2014b. Zircon U-Pb age, endogenic mineralization and petrogenesis of rare earth ore-bearing granite in Longnan, Jiangxi Province. Acta Geosci. Sin. 35, 719–725.

Zhao, W.W., Zhou, M.F., Li, Y.H.M., Zhao, Z., Gao, J.F., 2017. Genetic types, mineralization styles, and geodynamic settings of Mesozoic tungsten deposits in South China. J. Asian Earth Sci. 137, 109–140.

Zhou, X.M., Li, W.X., 2000. Origin of Late Mesozoic igneous rocks in Southeastern China: implications for lithosphere subduction and underplating of mafic magmas. Tectonophysics 326, 269–287.

Zhou, X.M., Sun, T., Shen, W.Z., Shu, L.S., Niu, Y.L., 2006. Petrogenesis of Mesozoic granitoids and volcanic rocks in South China: A response to tectonic evolution. Episodes 29, 26–33.